GPR Microwave Imaging Through An Innovative Multi-Frequency Deterministic Approach

M. Salucci, L. Poli, and A. Massa

Abstract

This work deals with the microwave imaging of the dielectric characteristics of buried targets in a lossy half-space. The solution of the arising inverse scattering (*IS*) problem is performed by processing wide-band ground penetrating radar (*GPR*) measurements through an innovative deterministic approach. More precisely, the developed *GPR-IS* technique is based on a multi-frequency (*MF*) scheme and integrates a conjugate-gradient (*CG*) solver within the iterative multi-scaling approach (*IMSA*). Some preliminary numerical results are shown in order to assess the effectiveness of the proposed methodology, as well as to compare it to a state-of-the-art deterministic approach based on a frequency hopping (*FH*) strategy.

1 Definitions

1.1 Glossary

- D_{inv}: investigation domain;
- D_{obs}: observation domain;
- N: number of discretization cells in D_{ind};
- V: number of views;
- M: number of measurement points;
- F: number of frequencies considered for the inversion;
- (x_v, y_v): coordinates of the v-th source $(v = 1, \ldots, V)$.
- (x_m^v, y_m^v): coordinates of the m-th measurement point for the v-th view v, $(m = 1, \ldots, M)$;
- $\varepsilon_{ra} = \frac{\varepsilon_a}{\varepsilon_0}$: relative electric permittivity for the upper half-space $(y > 0)$;
- σ_a: conductivity for the upper half-space $(y > 0)$;
- $\varepsilon_{rb} = \frac{\varepsilon_b}{\varepsilon_0}$: background relative electric permittivity;
- σ_b: background conductivity;

1.2 Contrast function at frequency f

The contrast function at frequency f is defined as

$$\tau_f(x, y) = \frac{\varepsilon_{eq}(x, y) - \varepsilon_{eqb}}{\varepsilon_0} = \Re\{\tau(x, y)\} + j\Im\{\tau(x, y)\}$$

where

- $\Re\{\tau(x, y)\} = [\varepsilon_r(x, y) - \varepsilon_{rb}]$;
- $\Im\{\tau(x, y)\} = \left[\frac{\sigma_b - \sigma(x,y)}{2\pi f \varepsilon_0}\right]$;
- $\varepsilon_{eq}(x, y) = \varepsilon_0 \varepsilon_r(x, y) - j\frac{\sigma(x,y)}{2\pi f}$;
- $\varepsilon_{eqb} = \varepsilon_0 \varepsilon_{rb} - j\frac{\sigma_b}{2\pi f}$;
- $\varepsilon_r(x, y)$: relative electric permittivity;
- $\sigma(x, y)$: conductivity;

NOTE: we assume that $\varepsilon_r(x, y)$ and $\sigma(x, y)$ are **not frequency dependent** (non-dispersive mediums).

1.3 $MF-CG$: Contrast function and reference frequency f_{ref}

The contrast function at a generic frequency f can be expressed by means of the contrast function computed for a selected reference frequency

$$f = f_{ref}$$

as follows

$$\tau_f = \Re\left\{\tau_{f_{ref}}\right\} + j\frac{f_{ref}}{f}\Im\left\{\tau_{f_{ref}}\right\}$$

1.4 $MF-CG$: Fitness definition

The functional minimized by the $MF-CG$ inversion algorithm is defined as

$$\Phi = \Phi_{state} + \Phi_{data}$$

where Φ_{state} and Φ_{data} are respectively the data and state terms of the cost function, defined as

$$\Phi_{state} = \frac{\sum_{f=1}^{F}\sum_{v=1}^{V}\sum_{n=1}^{N}\left|E_{inc}^{v,f}\left(x_n, y_n\right) - \widetilde{E}_{inc}^{v,f}\left(x_n, y_n\right)\right|^2}{\sum_{f=1}^{F}\sum_{v=1}^{V}\sum_{n=1}^{N}\left|E_{inc}^{v,f}\left(x_n, y_n\right)\right|^2}$$

$$\Phi_{data} = \frac{\sum_{f=1}^{F}\sum_{v=1}^{V}\sum_{m=1}^{M}\left|E_{scatt}^{v,f}\left(x_m^v, y_m^v\right) - \widetilde{E}_{scatt}^{v,f}\left(x_m^v, y_m^v\right)\right|^2}{\sum_{f=1}^{F}\sum_{v=1}^{V}\sum_{m=1}^{M}\left|E_{scatt}^{v,f}\left(x_m^v, y_m^v\right)\right|^2}$$

being

- $E_{inc}^{v,f}\left(x_n, y_n\right)$: measured incident field inside the n-th cell, for the v-th view at frequency f;
- $\widetilde{E}_{inc}^{v,f}\left(x_n, y_n\right)$: computed incident field inside the n-th cell, for the v-th view at frequency f;
- $E_{scatt}^{v,f}\left(x_m^v, y_m^v\right)$: measured scattered by the m-th measurement point, for the v-th view at frequency f;
- $\widetilde{E}_{scatt}^{v,f}\left(x_m^v, y_m^v\right)$: measured scattered by the m-th measurement point, for the v-th view at frequency f.

The unknowns of the inversion problem are

$$\mathbf{x} = \left\{\tau^{f_{ref}}\left(x_n, y_n\right); E_{tot}^{v,f}\left(x_n, y_n\right)\right\} \qquad n = 1, ..., N; v = 1, ..., V; f = 1, ..., F$$

1.5 Time-domain SNR definition on the external total field

Since data is collected through a GPR system in time-domain, a white Gaussian noise is applied to the measured total field in time domain.

The measured total field E_{tot} is corrupted in the time domain by the desired quantity of noise following this definition of SNR:

$$SNR = 10log_{10}\frac{\sum_{v=1}^{V}\sum_{m=1}^{M}\int_{-\infty}^{\infty}\left|E_{tot}^{v}\left(x_m^v, y_m^v, t\right)\right|^2 dt}{\sum_{v=1}^{V}\sum_{m=1}^{M}\int_{-\infty}^{\infty}\left|n^{v}\left(x_m^v, y_m^v, t\right)\right|^2 dt}$$

where

- $E_{tot}^{v}\left(x_m^v, y_m^v, t\right)$ is the measured total field by the m-th probe under the v-th view, at time instant t;
- $n^{v}\left(x_m^v, y_m^v, t\right)$ is the noise component affecting the total field measured total field by the m-th probe under the v-th view, at time instant t;

1.5.1 Measuring the resulting SNR (on E_{scatt}) in the frequency domain

After the total measured field E_{tot} has been corrupted in time-domain by a given quantity of noise (following the above definition of SNR), the scattered field is obtained - in the frequency domain - as the difference between the transformed total and incident fields. The resulting SNR at a given frequency f on the external scattered field can be estimated as the average SNR measured over all the views $v = 1, ..., V$:

$$SNR\left\{E_{scatt}\left(f\right)\right\} = \frac{1}{V}\sum_{v=1}^{V} SNR\left\{E_{scatt}^{v}\left(f\right)\right\}$$

where $SNR\left\{E_{scatt}^{v}\left(f\right)\right\}$ represents the Signal-To-Noise Ratio measured on the scattered field in frequency domain for a given view v $(v = 1, ..., V)$ and it can be measured as:

$$SNR\left\{E_{scatt}^{v}\left(f\right)\right\} = 10log_{10}\left\{\frac{\sum_{m=1}^{M}\left|E_{scatt}^{v,noiseless}\left(x_m^v, y_m^v; f\right)\right|^2}{\sum_{m=1}^{M}\left|n^{v}\left(x_m^v, y_m^v; f\right)\right|^2}\right\}$$

where the noise component $n^{v}\left(x_m, y_m; f\right)$ on a given measurement point m is computed as the difference between the noisy and the noiseless realizations of the scattered field measured on that point (for a given view index v):

$$n^{v}\left(x_m, y_m; f\right) = E_{scatt}^{v}\left(x_m^v, y_m^v; f\right) - E_{scatt}^{v,noiseless}\left(x_m^v, y_m^v; f\right)$$

1.6 Reconstruction errors

The following integral error is defined

$$\Xi_{reg} = \frac{1}{N_{reg}} \sum_{n=1}^{N_{reg}} \frac{|\tau_n^{act} - \tau_n^{rec}|}{|\tau_n^{act} + 1|}$$

where reg indicates if the error computation covers

- the overall investigation domain ($reg \Rightarrow tot$),
- the actual scatterer's support ($reg \Rightarrow int$),
- or the background region ($reg \Rightarrow ext$).

2 $IMSA - MF - CG$: stopping criteria

The $IMSA - MF - CG$ iterative process is stopped at step s-th (which becomes s^{best}) if one of the following conditions holds true:

1. The side of the zoomed reconstruction domain for the next step ($L_{(s+1)}$) is such that:

$$\frac{\left|L_{(s+1)} - L_{(s)}\right|}{L_{(s)}} < \eta_{th}$$

   being $L_{(s)}$ the side of the reconstruction domain at step s-th and η_{th} a proper threshold, with $0 < \eta_{th} < 1$;

2. The maximum number of $IMSA - MF - CG$ steps has been reached ($s = S$).

Two parameters will thus determine when the $IMSA - MF - CG$ iterative process should be stopped at each intermediate frequency step:

- the threshold: η_{th};
- the maximum number of $MF - IMSA - CG$ steps: S.

A note on the threshold η_{th}

The following considerations should be taken into consideration when setting the threshold η_{th}:

1. If η_{th} is large, the condition $\frac{\left|L_{(s+1)} - L_{(s)}\right|}{L_{(s)}} < \eta_{th}$ will stop the $IMSA - MF - CG$ after few steps. In fact, if η_{th} is set to a very high value (e.g., $\eta_{th} = 0.9$), probably no $IMSA - MF - CG$ steps will be performed after the first one (and therefore $s^{best} = 1$ for each frequency step).
2. If η_{th} is small, the condition $\frac{\left|L_{(s+1)} - L_{(s)}\right|}{L_{(s)}} < \eta_{th}$ will stop the $IMSA - MF - CG$ after a lot of steps. In fact, if η_{th} is set to a very low value (e.g., $\eta_{th} = 0.001$), $IMSA - MF - CG$ will always iterate until the maximum number of steps (S) is reached (and therefore $s^{best} = S$ for each frequency step).

3 Multi-Frequency (MF) vs. Frequency-Hopping (FH)

3.1 Goal of this section

The goal of this section is to perform a numerical comparison on a selected test case between

1. **Frequency-Hopping approaches**
   (a) $FH - BARE - CG$;
   (b) $FH - IMSA - CG$;
2. **Multi-Frequency approaches**
   (a) $BARE - MF - CG$;
   (b) $IMSA - MF - CG$.

3.2 Parameters

Background

Inhomogeneous and nonmagnetic background composed by two half spaces

- Upper half space ($y > 0$ - air): $\varepsilon_{ra} = 1.0$, $\sigma_a = 0.0$;
- Lower half space ($y < 0$ - soil): $\varepsilon_{rb} = 4.0$, $\sigma_b = 10^{-3}$[S/m];

Investigation domain (D_{inv})

- Side: $L_{D_{inv}} = 0.8$ [m];
- Barycenter: $\left(x_{bar}^{D_{inv}}, y_{bar}^{D_{inv}}\right) = (0.00, -0.4)$ [m];

FDTD Direct solver parameters (*GPRMax2D*)

- Side of the simulated domain: $L = 6$ [m];
- Number of cells: $N^{FDTD} = 750 \times 750 = 5.625 \times 10^5$;
- Side of the *FDTD* cells $l^{FDTD} = 0.008$ [m];
- Simulation time window: $T^{FDTD} = 20 \times 10^{-9}$ [sec];
- Time step: $\Delta t^{FDTD} = 1.89 \times 10^{-11}$ [sec];
- Number of time samples: $N_t^{FDTD} = 1060$;
- Boundary conditions: Perfectly matched layer (*PML*);
- Source type: Gaussian mono-cycle (first Gaussian pulse derivative, called “Ricker” in *GPRMax2D*)
  - Central frequency: $f_0 = 300$ [MHz];
  - Source amplitude: $A = 1.0$ [A];

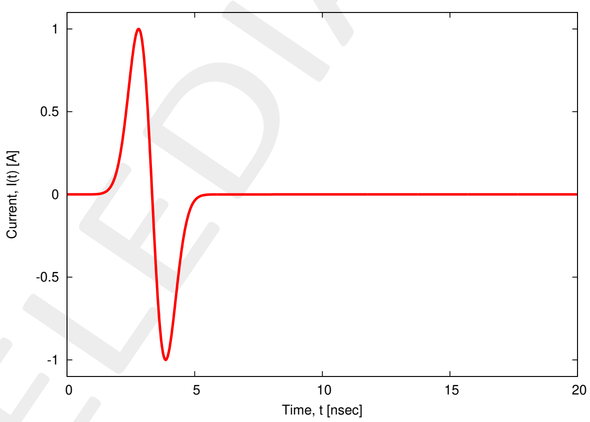

(a)

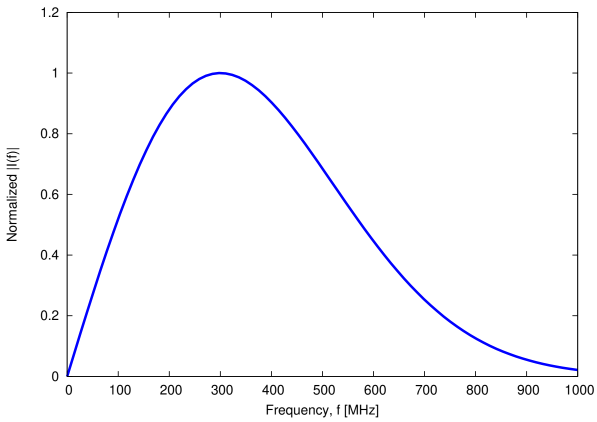

(b)

Figure 1: *GPRMax2D* excitation signal. (a) Time behavior, (b) normalized frequency spectrum.

Frequency parameters

- Frequency range: $f \in [f_{min}, f_{max}] = [200.0, 600.0]$ [MHz];
- Considered frequencies:

f [MHz]	λ_a [m]	λ_b [m]	f [MHz]
200.0	1.50	0.75	200.5
300.0	1.00	0.50	297.6
400.0	0.75	0.37	401.1
500.0	0.60	0.30	498.1
600.0	0.50	0.25	601.6

Table 1: Considered frequencies and corresponding wavelength in the upper medium (λ_a, free space) and in the lower medium (λ_b, soil). f^* is the nearest frequency sample available from transformed time-domain data, and represents the real frequency considered by the inversion algorithm.

Scatterer

- Barycenter: $(x_{obj}, y_{obj}) = (-0.08, -0.24)$ [m];
- Side: $L_{obj,x} = L_{obj,y} = 0.16$ [m];
- Electromagnetic properties: $\varepsilon_{r,obj} = 5.0$, $\sigma_{obj} = 10^{-3}$ [S/m] ($\sigma_{obj} = \sigma_b$);
- Contrast function: $\tau = 1.0 + j0.0$

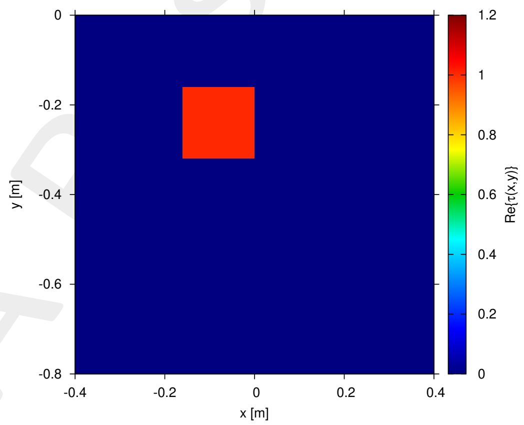

Figure 2: Actual object: offset square cylinder $\tau = 1.0$.

Measurement setup

- Number of views (sources): $V = 20$;
  - $\min\{x_v\} = -0.564$ [m], $\max\{x_v\} = 0.5$ [m];
  - height: $y_v = 0.1$ [m], $\forall v = 1, \dots, V$;
- Number of measurement points: $M = 19$;
  - $\min\{x_m\} = -0.564$ [m], $\max\{x_m\} = 0.5$ [m];
  - height: $y_m = 0.1$ [m], $\forall m = 1, \dots, M$;

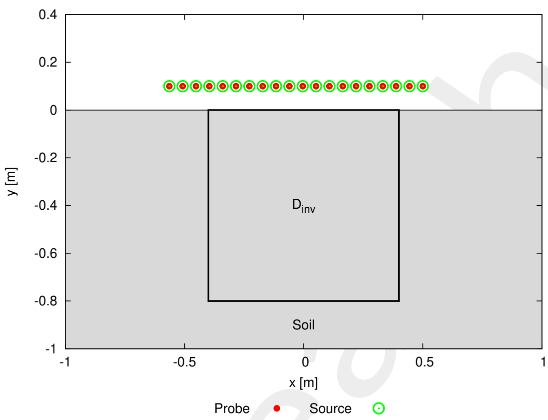

Figure 3: Location of the measurement points ($M = 19$) and of the sources ($V = 20$). Only one source is active for each view.

Inverse solver parameters

- **Shared parameters**
  - Weight of the state term of the functional: 1.0;
  - Weight of the data term of the functional: 1.0;
  - Weight of the penalty term of the functional: 0.0;
  - Convergence threshold: 10^{-8};
  - Maximum number of iterations: $I_{max} = 400$;
  - Variable ranges:
    * $\varepsilon_r \in [4.0, 6.0]$, $\sigma \in [0.0, 0.002]$ S/m;
    * $\Re\{E_{tot}^{int}\} \in [-25, 25]$, $\Im\{E_{tot}^{int}\} \in [-25, 25]$;

- **Frequency Hopping (FH) approaches**
  - $FH-BARE-CG$ **(FH-FULL) parameters**
    - Number of cells: $N = 20 \times 20 = 400$;
    - Side of the cells: $l = 0.04$ [m] $\rightarrow \sim \lambda_b/10$ discretization @ $f_{central} = 400$ [MHz];
  - $FH-IMSA-CG$ **(FH-FULL Area-Based) parameters**
    - Maximum number of $IMSA$ steps: $S = 6$;
    - Side ratio threshold: $\eta_{th} = 0.2$;
    - Degrees of freedom:
      - Considered frequency: $f_{central} = 400$ [MHz], $\lambda_b = 0.37$ [m];
      - $\#DOF = \frac{(2ka)^2}{2} = \frac{\left(2\times\frac{2\pi}{\lambda_b}\times\frac{L\sqrt{2}}{2}\right)^2}{2} = 4\pi^2\left(\frac{L}{\lambda_b}\right)^2 = 4\pi^2\left(\frac{0.8}{0.37}\right)^2 \simeq 184.4.$
      - Number of cells: $N = 196 = 14 \times 14$;
      - Number of cells for each side: $N_L = 14$;
      - Side of the cells: $l = 0.057$ [m];
    - Zoom Factor $= 0.1$;
- **Multi-Frequency (MF) approaches**
  - $BARE-MF-CG$ **parameters**
    - Number of cells: $N = 20 \times 20 = 400$;
    - Side of the cells: $l = 0.04$ [m] $\rightarrow \sim \lambda_b/10$ discretization @ $f_{central} = 400$ [MHz];
    - Reference frequency: $f_{ref} = f_{central} = 400$ [MHz];
  - $IMSA-MF-CG$ **parameters**
    - Maximum number of $IMSA$ steps: $S = 6$;
    - Side ratio threshold: $\eta_{th} = 0.2$;
    - Degrees of freedom:
      - Considered frequency: $f_{central} = 400$ [MHz], $\lambda_b = 0.37$ [m];
      - $\#DOF = \frac{(2ka)^2}{2} = \frac{\left(2\times\frac{2\pi}{\lambda_b}\times\frac{L\sqrt{2}}{2}\right)^2}{2} = 4\pi^2\left(\frac{L}{\lambda_b}\right)^2 = 4\pi^2\left(\frac{0.8}{0.37}\right)^2 \simeq 184.4.$
      - Number of cells: $N = 196 = 14 \times 14$;
      - Number of cells for each side: $N_L = 14$;
      - Side of the cells: $l = 0.057$ [m];
    - Zoom Factor $= 0.1$;

Signal to noise ratio on $E_{tot}(t)$:

- Noiseless Data;
- $SNR = 40$ [dB] ($SNR_{average}\{E_{scatt}(f)\} \simeq 23$ [dB]).

3.3 Retrieved contrast

3.3.1 Noiseless Data

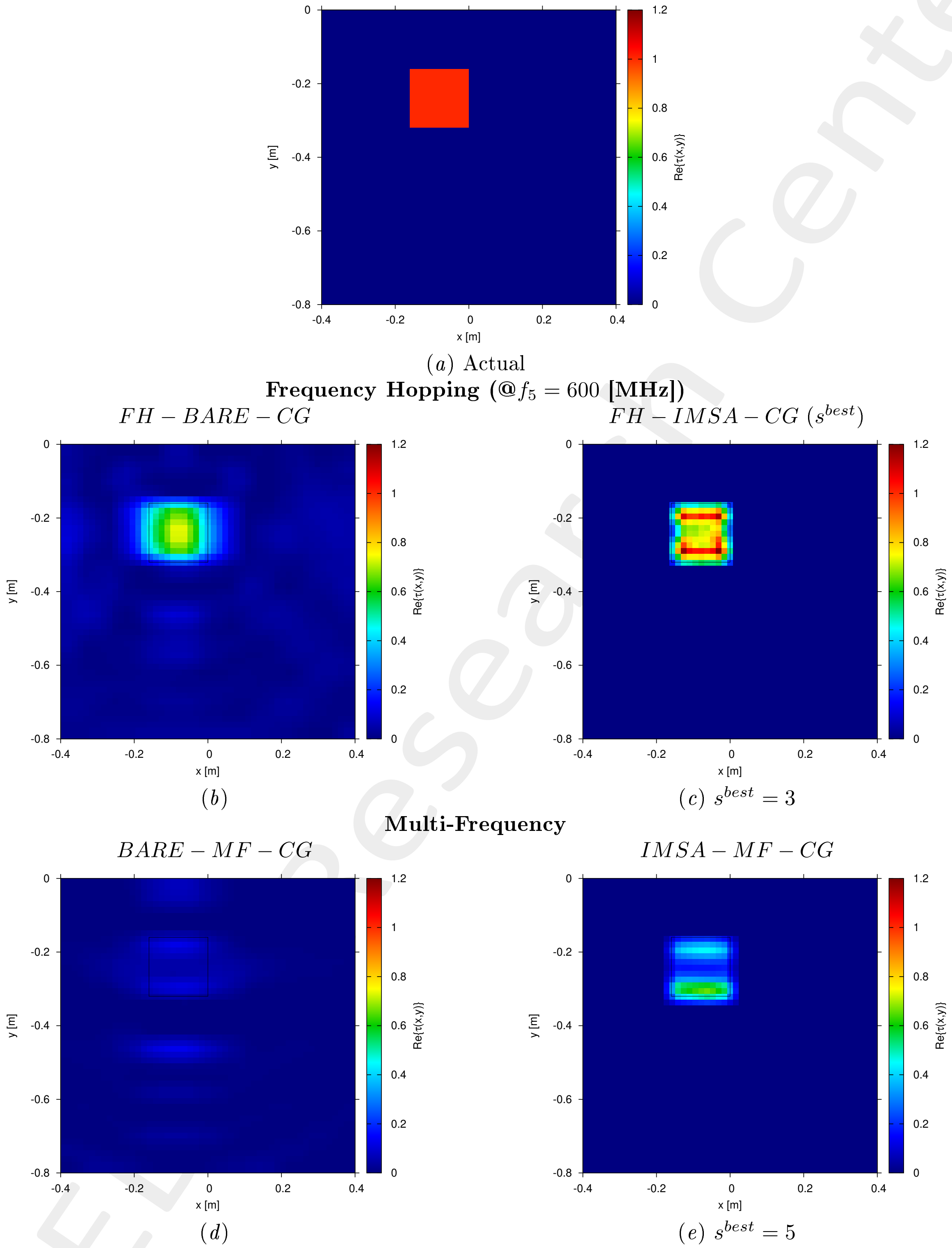

Figure 4: **Noiseless Data -** (a) Actual and retrieved contrast by $(b)(c)$ FH techniques (last frequency step) and by $(d)(e)$ MF techniques.

3.3.2 Noisy Data - $SNR = 40$ [dB]

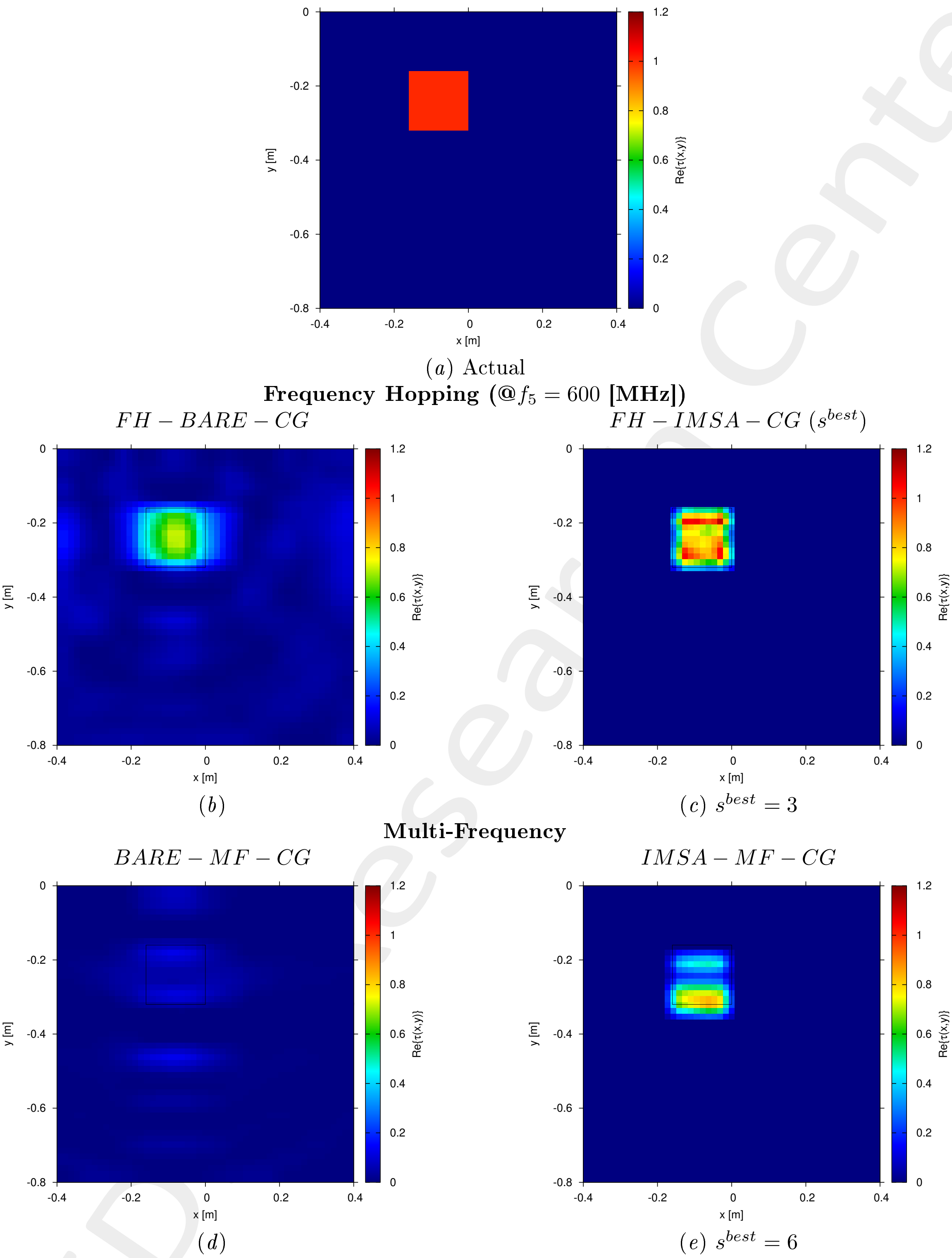

Figure 5: **Noisy Data ($SNR = 40$ [dB]) -** (a) Actual and retrieved contrast by $(b)(c)$ FH techniques (last frequency step) and by $(d)(e)$ MF techniques.

3.4 $IMSA-MF-CG$: Intermediate results

3.4.1 Noiseless Data

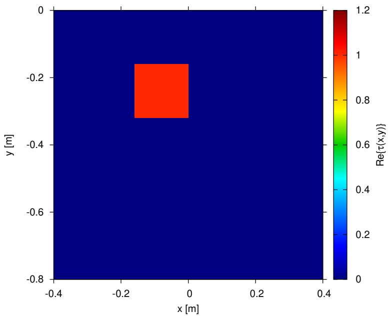

(a) Actual

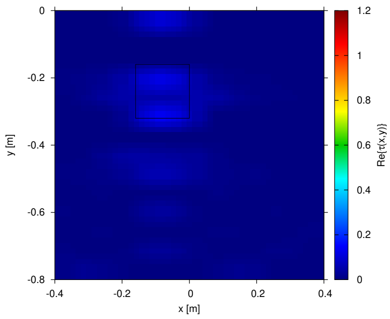

(b) $s = 1$

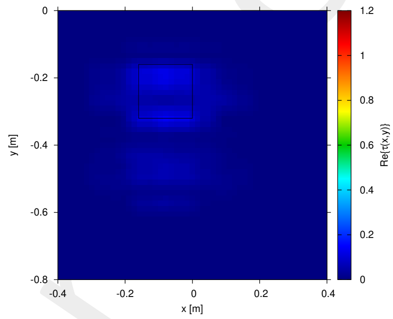

(c) $s = 2$

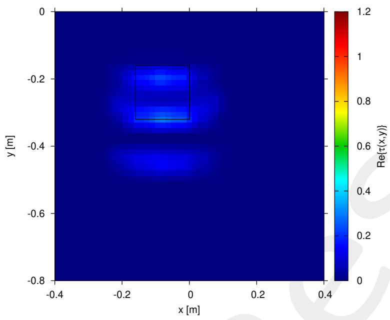

(d) $s = 3$

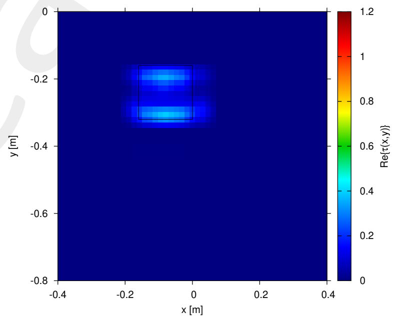

(e) $s = 4$

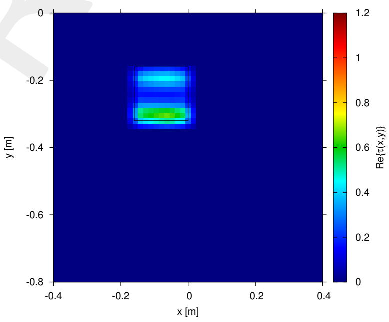

(f) $s = 5 = s^{best}$

Figure 6: **Noiseless Data -** (a) Actual and $(b)(f)$ retrieved contrast by $IMSA-MF-CG$ at each intermediate step.

3.4.2 Noisy Data - $SNR = 40$ [dB]

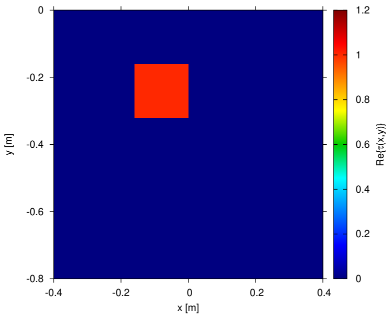

(a) Actual

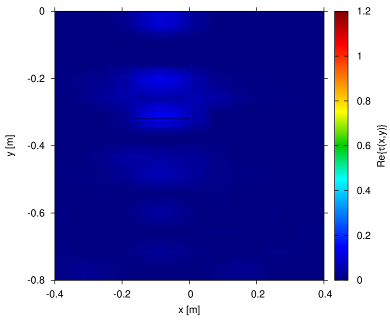

(b) $s = 1$

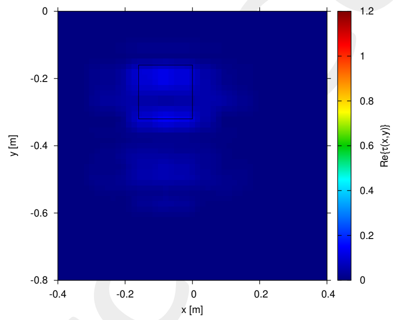

(c) $s = 2$

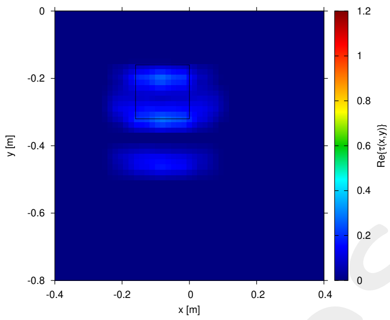

(d) $s = 3$

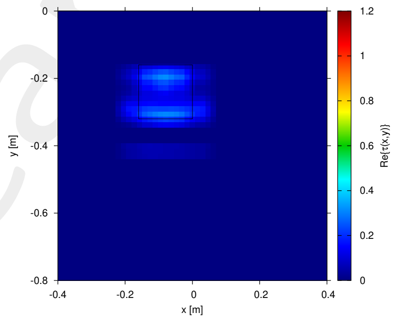

(e) $s = 4$

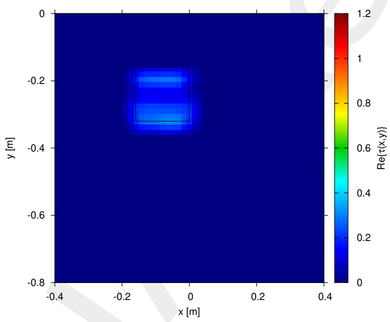

(f) $s = 5$

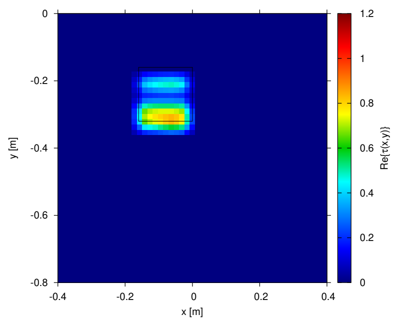

(g) $s = S = 6$

Figure 7: **Noisy Data ($SNR = 40$ [dB]) -** (a) Actual and $(b)(f)$ retrieved contrast by $IMSA - MF - CG$ at each intermediate step.

3.4.3 Intermediate reconstruction errors

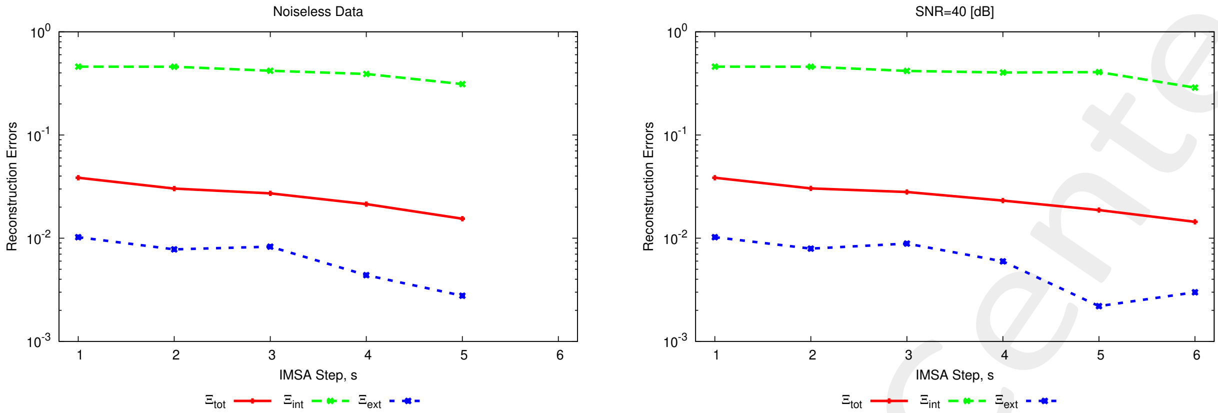

(b) Noiseless Data (c) $SNR = 40$ [dB]

Figure 8: $IMSA - MF - CG$ - Reconstruction errors at each intermediate $IMSA$ step $(s = 1, ..., s^{best})$.

More information on the topics of this document can be found in the following list of references.

References

[1] P. Rocca, M. Benedetti, M. Donelli, D. Franceschini, and A. Massa, "Evolutionary optimization as applied to inverse scattering problems," *Inverse Probl.*, vol. 25, no. 12, pp. 1-41, 2009 (DOI: 10.1088/0266-5611/25/12/123003).

[2] P. Rocca, G. Oliveri, and A. Massa, "Differential Evolution as applied to electromagnetics," *IEEE Antennas Propag. Mag.*, vol. 53, no. 1, pp. 38-49, Feb. 2011 (DOI: 10.1109/MAP.2011.5773566).

[3] M. Salucci, G. Oliveri, and A. Massa, "GPR prospecting through an inverse scattering frequency-hopping multi-focusing approach," *IEEE Trans. Geosci. Remote Sens.*, vol. 53, no. 12, pp. 6573-6592, Dec. 2015 (DOI: 10.1109/TGRS.2015.2444391).

[4] M. Salucci, L. Poli, N. Anselmi and A. Massa, "Multifrequency particle swarm optimization for enhanced multiresolution GPR microwave imaging," *IEEE Trans. Geosci. Remote Sens.*, vol. 55, no. 3, pp. 1305-1317, Mar. 2017 (DOI: 10.1109/TGRS.2016.2622061).

[5] A. Massa, P. Rocca, and G. Oliveri, "Compressive sensing in electromagnetics - A review," *IEEE Antennas Propag. Mag.*, pp. 224-238, vol. 57, no. 1, Feb. 2015 (DOI: 10.1109/MAP.2015.2397092).

[6] A. Massa and F. Texeira, "Guest-Editorial: Special Cluster on Compressive Sensing as Applied to Electromagnetics," *IEEE Antennas Wireless Propag. Lett.*, vol. 14, pp. 1022-1026, 2015 (DOI: 10.1109/LAWP.2015.2425011).

[7] N. Anselmi, G. Oliveri, M. Salucci, and A. Massa, "Wavelet-based compressive imaging of sparse targets," *IEEE Trans. Antennas Propag.*, vol. 63, no. 11, pp. 4889-4900, Nov. 2015 (DOI: 10.1109/TAP.2015.2444423).

[8] G. Oliveri, N. Anselmi, and A. Massa, "Compressive sensing imaging of non-sparse 2D scatterers by a total-variation approach within the Born approximation," *IEEE Trans. Antennas Propag.*, vol. 62, no. 10, pp. 5157-5170, Oct. 2014 (DOI: 10.1109/TAP.2014.2344673).

[9] T. Moriyama, G. Oliveri, M. Salucci, and T. Takenaka, "A multi-scaling forward-backward time-stepping method for microwave imaging," *IEICE Electron. Expr.*, vol. 11, no. 16, pp. 1-12, Aug. 2014 (DOI: 10.1587/elex.11.20140578).

[10] T. Moriyama, M. Salucci, M. Tanaka, and T. Takenaka, "Image reconstruction from total electric field data with no information on the incident field," *J. Electromagnet. Wave.*, vol. 30, no. 9, pp. 1162-1170, 2016 (DOI: 10.1080/09205071.2016.1182876).

[11] F. Viani, L. Poli, G. Oliveri, F. Robol, and A. Massa, "Sparse scatterers imaging through approximated multi-task compressive sensing strategies," *Microw. Opt. Technol. Lett.*, vol. 55, no. 7, pp. 1553-1557, Jul. 2013 (DOI: 10.1002/mop.27612).

[12] M. Salucci, L. Poli, and A. Massa, "Advanced multi-frequency GPR data processing for non-linear deterministic imaging," *Signal Processing - Special Issue on 'Advanced Ground-Penetrating Radar Signal-Processing Techniques*,' vol. 132, pp. 306-318, Mar. 2017 (DOI: 10.1016/j.sigpro.2016.06.019).

[13] M. Salucci, N. Anselmi, G. Oliveri, P. Calmon, R. Miorelli, C. Reboud, and A. Massa, “Real-time NDT-NDE through an innovative adaptive partial least squares SVR inversion approach,” *IEEE Trans. Geosci. Remote Sens.*, vol. 54, no. 11, pp. 6818-6832, Nov. 2016 (DOI: 10.1109/TGRS.2016.2591439).

[14] L. Poli, G. Oliveri, and A. Massa, “Imaging sparse metallic cylinders through a local shape function bayesian compressing sensing approach,” *J. Opt. Soc. Am. A*, vol. 30, no. 6, pp. 1261-1272, Jun. 2013 (DOI: 10.1364/JOSAA.30.001261).